

000  
001  
002  
003  
004  
005  
006  
007  
008  
009  
010  
011  
012  
013  
014  
015  
016  
017  
018  
019  
020  
021  
022  
023  
024  
025  
026  
027  
028  
029  
030  
031  
032  
033  
034  
035  
036  
037  
038  
039  
040  
041  
042  
043  
044  
045  
046  
047  
048  
049  
050  
051  
052  
053  

# SPACE GROUP CONDITIONAL FLOW MATCHING

**Anonymous authors**

Paper under double-blind review

## ABSTRACT

Inorganic crystals are periodic, highly-symmetric arrangements of atoms in three-dimensional space. Their structures are constrained by the symmetry operations of a crystallographic *space group* and restricted to lie in specific affine subspaces known as *Wyckoff positions*. The frequency an atom appears in the crystal and its rough positioning are determined by its Wyckoff position. Most generative models that predict atomic coordinates overlook these symmetry constraints, leading to unrealistically high populations of proposed crystals exhibiting limited symmetry. We introduce Space Group Conditional Flow Matching, a novel generative framework that samples significantly closer to the target population of highly-symmetric, stable crystals. We achieve this by conditioning the entire generation process on a given space group and set of Wyckoff positions; specifically, we define a conditionally symmetric noise base distribution and a group-conditioned, equivariant, parametric vector field that restricts the motion of atoms to their initial Wyckoff position. Our form of group-conditioned equivariance is achieved using an efficient reformulation of *group averaging* tailored for symmetric crystals. Importantly, it reduces the computational overhead of symmetrization to a negligible level. [We achieve state of the art results on de novo generation and ground truth Wyckoff conditioned crystal structure prediction benchmarks.](#)

## 1 INTRODUCTION

Crystals are solid materials characterized by a periodic arrangement of their constituent atoms. The crystalline structure is fundamentally represented by three components: lattice parameters (defining the geometry of the repeating unit cell), fractional coordinates (specifying the position of each atom within the cell), and the identity of the atom at each location. The discovery of novel crystalline structures is critical for material design and recent progress in generative modeling has demonstrated a promising approach to this problem. However, most existing generative methods overlook key crystallographic properties, the space group and Wyckoff positions, making it challenging for them to generate non-trivial symmetric crystals.

A crystal’s space group, a subgroup of the Euclidean group  $E(n)$ , fully describes the symmetry of the atoms arranged within the unit cell. Beyond its correlation with many optical, electrical, magnetic, and structural properties (Chen et al., 2022; Tang et al., 2019; Malgrange et al., 2014; Yang, 2005), the space group imposes constraints on atomic locations and lattice structure. These manifests in form of Wyckoff positions, which are sets of symmetrically equivalent points within a unit cell. More generally, the Wyckoff positions of a space group partition the unit cell according to the structure of the orbits induced by the group (see fig. 2 for a 2D example).

In this work, we develop a generative model that samples crystals conditioned on a given space group and associated Wyckoff positions. This approach offers two key benefits: (1) it provides greater control over the structure and symmetry of the generated crystals, and (2) it can leverage the lower-dimensional constraints imposed by Wyckoff positions for improving generation. In contrast to prior methods that incorporate space group information but rely on projection steps to correct atomic placements (Jiao et al., 2024; Levy et al., 2025), our model is designed to inherently preserve the assignment of atoms to their designated Wyckoff positions throughout the generation process.

Our proposed model, *Space Group Conditional Flow Matching* (SGFM), is based on the *Flow Matching* (FM) generative framework (Albergo & Vanden-Eijnden, 2022; Liu et al., 2022; Lipman et al., 2022). We chose the FM framework for two key reasons: it allows us to use customized source

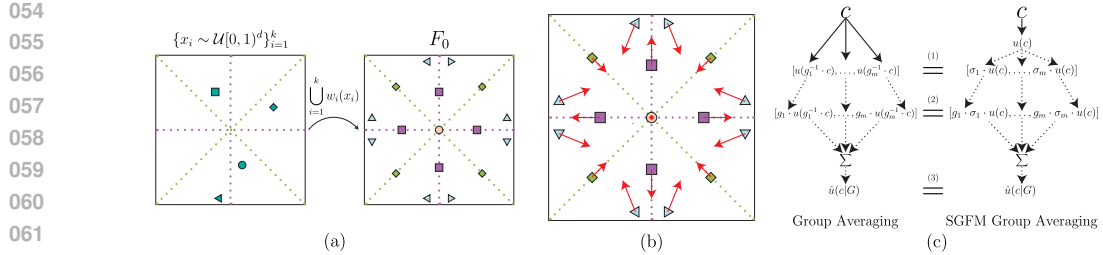


Figure 1: Visualization of the main components of SGFM. (a) Wyckoff position noise prior. General points are sampled randomly and projected according to the conditioned Wyckoff positions. (b) Space group equivariant vector field. The equivariance of the model combined with the  $G$ -symmetry of the input crystal ensures that atoms preserve their symmetry structure. (c) Comparison between standard group averaging and our optimized formulation. The  $G$ -symmetry of the input crystal allows space group operations to be replaced by their corresponding permutations (denoted using  $\sigma$ ). When combined with the  $S_n$ -equivariance of  $u$ , this reduces the number of required forward passes per crystal. For visualization purposes, heavy arrows indicate expensive model forward passes.

distributions and provides known conditions for generating data that respects specified symmetries (Köhler et al., 2020). Based on these advantages, we designed SGFM with two main components: A space group and Wyckoff position conditioned noise prior, which have positive support only for crystal structures that adhere to the symmetry constraints described by the Wyckoff positions; A group conditioned equivariant vector field, which is a single neural network architecture that is able to support arbitrary space group equivariance. Equivariance is achieved through Group Averaging (GA) (Yarotsky, 2022), a symmetrization technique that projects arbitrary functions onto their equivariant versions. Although GA is typically computationally expensive and impractical, we introduce an efficient formulation tailored for symmetric crystals, reducing the computational overhead of the symmetrization operator to a negligible level.

The main contributions of this work are as follows:

- We formalized the problem of symmetric crystal generation in terms of distributional symmetry properties (section 3.1), and extended the conditions introduced by Köhler et al. (2020) to enable flow-based models to sample from such distributions (section 3.2).
- We instantiate this flow model as SGFM (section 3.3), which consists of a noise prior conditional on Wyckoff position along with a space group-equivariant vector field, ensuring that the generated crystals preserve the specified symmetries.
- We propose a novel and efficient implementation of GA for symmetric crystals, equivalent in output to the standard GA but significantly more efficient (see fig. 1 (c)), practically minimizing the computational burden of symmetrization for symmetric crystals.
- SGFM achieves state-of-the-art performance on de novo generation (DNG). Compared with a baseline that also receives the ground truth Wyckoff positions, SGFM achieves SOTA on a crystal structure prediction (CSP) benchmark in which atom types are given.

## 2 PRELIMINARIES

**Equivariance & Invariance.** A function  $\varphi : \mathcal{X} \rightarrow \mathcal{Y}$  is equivariant with respect to a group  $G$  if the action of any group element on the input corresponds to a consistent transformation of the output. Equivariance implies  $\varphi(g \cdot x) = g \cdot \varphi(x)$  for all  $x \in \mathcal{X}$  and  $g \in G$ . Invariance is a simplified case of equivariance, with all  $g \in G$  mapping to a trivial group action on the output space  $\varphi(g \cdot x) = \varphi(x)$ . Invariance and equivariance also extend to group products: Let  $(g_1, g_2) \in G_1 \times G_2$ ,  $\varphi$  is  $G_1 \times G_2$  equivariant if  $\varphi((g_1, g_2) \cdot x) = (g_1, g_2) \cdot \varphi(x)$ . Additionally,  $G$ -invariant distributions refer to distributions which have an  $G$ -invariant density function. We will use this to construct SGFM.

**Crystal Representation.** A crystal can be represented using the tuple  $c' = (\mathbf{L}, \mathbf{F}, \mathbf{A}) \in \mathcal{C}'$ , where  $\mathbf{L} \in \mathbb{R}^{3 \times 3}$  is a positive-determinant, invertible matrix defining the lengths, angles, and orientation of the positive-volume unit cell;  $\mathbf{F} \in [0, 1]^{n \times 3}$  denotes the fractional coordinates of  $n$  atoms within the unit cell; and  $\mathbf{A} \in \{0, 1\}^{n \times h}$  is a one-hot matrix indicating the atom types in  $\mathbf{F}$  from a set of  $h$

108 atom types. We adopt the space group–conditioned lattice parameterization proposed by Jiao et al.  
109 (2024), which replaces  $\mathbf{L}$  with a rotation-invariant vector  $k \in \mathbb{R}^6$  of coefficients of a symmetric  
110 matrix basis, and represent a crystal as  $c = (k, \mathbf{F}, \mathbf{A}) \in \mathcal{C}$ . Further details provided in appendix C.  
111

112 **Symmetries & Crystals.** Our method focuses on how symmetry groups act on crystals. The per-  
113 mutation group  $S_n$  acts on  $c$  by permuting the rows of  $\mathbf{F}$  and  $\mathbf{A}$ . Namely, if  $\sigma \in S_n$  is represented  
114 by a permutation matrix  $\mathbf{P} \in \{0, 1\}^{n \times n}$  then  $\sigma \cdot c = (k, \mathbf{P}\mathbf{F}, \mathbf{P}\mathbf{A})$ . The group of isometries of  $\mathbb{R}^3$   
115 known as the Euclidean group  $E(3)$ , acts on  $c$  by applying an orthogonal transformation  $\mathbf{R} \in O(3)$   
116 and a translation  $\tau \in \mathbb{R}^3$  to the fractional coordinates. For a group element  $g = (\mathbf{R}, \tau) \in E(3)$ ,  
117 the action is defined as  $g \cdot c = (k, \mathbf{F}\mathbf{R}^T + \mathbf{1}_n\tau^T - \lfloor \mathbf{F}\mathbf{R}^T + \mathbf{1}_n\tau^T \rfloor, \mathbf{A})$  where  $\mathbf{1}_n \in \{1\}^n$  is a  
118 column vector of ones and  $\lfloor \cdot \rfloor$  is the element-wise floor function. We further specify the action of  
119 the product group on  $c$ . Let  $(g, \sigma) \in G \times S_n$ , we define  $(g, \sigma) \cdot c := g \cdot (\sigma \cdot c)$ . Puny et al. (2021)  
120 showed that if  $G \leq E(3)$  then  $g \cdot (\sigma \cdot c) = \sigma \cdot (g \cdot c)$ , i.e., the operators commute.

121 **Space Groups.** The space group concept formalizes the  
122 intrinsic symmetry of a crystal. If  $c \in \mathcal{C}$  is a crystal  
123 and  $G \leq E(3)$  is its symmetry space group, then for  
124 any  $g \in G$  there exist a permutation  $\sigma \in S_n$  that sat-  
125 isfies the relation  $g \cdot c = \sigma \cdot c$ , a property we will de-  
126 note as  $G$ -symmetry. In essence, any action of the space  
127 group is equivalent to a permutation of the atom positions,  
128 fig. 2 visualizes this property using a 2D example. The  
129 p4mm symmetry group includes rotations by angles of  
130  $\frac{\pi z}{2}$  for  $z \in \mathbb{Z}$ . The corresponding permutation is invis-  
131 ible, without fabricated labels, because it rearranges the  
132 positions of identical shapes. Two Crystals  $c_1, c_2 \in \mathcal{C}$   
133 are *Mutually G-Symmetric* if every space group element  
134  $g$  corresponds to the same permutation  $\sigma$  on both crys-  
135 tals. Formally,  $c_1$  and  $c_2$  are mutually  $G$ -symmetric if  
136  $g \cdot c_1 = \sigma \cdot c_1 \iff g \cdot c_2 = \sigma \cdot c_2$ . There exist 230 dis-  
137 tinct space groups in three-dimensional crystallography.  
138 Owing to the intrinsic periodicity of crystal structures,  
139 all corresponding subgroups are finite subgroups of the  
140 Euclidean group  $E(3)$ . For non-orthogonal lattice struc-  
141 tures, the space group acts on fractional coordinates as elements of the special affine group  $SA(3)$ ,  
142 rather than  $E(3)$ , fig. 5 demonstrates this in 2D. In simpler terms, we apply the group action after  
143 mapping every lattice to the cube using  $\mathbf{L}^{-1}$ .

144 **Wyckoff Positions.** Intuitively, Wyckoff positions of a space  
145 group  $G$  indicate regions with specific symmetry properties.  
146 Atoms in general position occupy the least symmetric position  
147 in the crystal, appear most frequently in the unit cell, and en-  
148 joy the fewest restrictions on their coordinates. Meanwhile,  
149 atoms in one of the several special positions occupy a region  
150 of higher symmetry, appear less frequently in the unit cell, and  
151 are restricted to lie in low-dimensional affine subspaces. More  
152 formally, a Wyckoff position  $w$ , is defined by a set of  $|w| = m$   
153 affine projections  $\{(\mathbf{V}_i, \tau_i)\}_{i=1}^m$  onto the corresponding affine  
154 subspaces, with  $\mathbf{V}_i \in \mathbb{R}^{3 \times 3}$  and  $\tau_i \in \mathbb{R}^3$ . We denote projection  
155 of  $f \in [0, 1]^3$  onto each of these  $m$  affine subspaces by,  
156 
$$w(f) := \{\mathbf{V}_i f + \tau_i - \lfloor \mathbf{V}_i f + \tau_i \rfloor\}_{i=1}^m. \quad (1)$$

157 If  $w$  is a Wyckoff position of a space group  $G$ , for every  $y \in w(f)$  we have the property  $w(f) =$   
158  $G \cdot y$  where  $G \cdot y := \{g \cdot y \mid g \in G\}$  denotes the *orbit* of  $y$  under  $G$ . This is visualized in fig. 3;  
159 it illustrates how  $f$  is mapped to an orbit induced by  $G$  through  $w$ . Each affine transformation  
160  $(\mathbf{V}_i, \tau_i)$  identifies with a subgroup  $G' \leq G$  that fixes points on its corresponding image. Namely,  
161  $y_i = \mathbf{V}_i f + \tau_i - \lfloor \mathbf{V}_i f + \tau_i \rfloor$  for some  $f \in [0, 1]^3$  if and only if  $G' = \{g \in G \mid g \cdot y_i = y_i\}$ . That  
162 means that  $G' = G_{y_i}$ , the *site-symmetry* (stabilizer) group of  $y_i$ . We define the crystal  $c$  (with  
163 fractional coordinates  $\mathbf{F}$ ) to be  $\mathcal{W}$ -constructable with respect to  $\mathcal{W} = (w_1, \dots, w_k)$  if there exist  $k$   
164 points  $\{x_i \in [0, 1]^3\}_{i=1}^k$  in the unit cell such that  $\mathbf{F} = \bigcup_{i=1}^k w_i(x_i)$  up to a permutation.

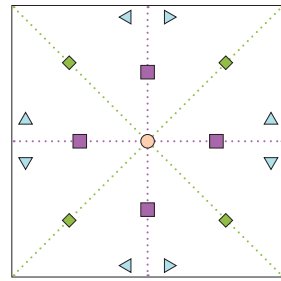


Figure 2: A 2D example of a unit cell with p4mm symmetry. Applying a group element to this set permutes “atoms” of the same type (shape and color). The symmetry divides the unit cell (black box) into four Wyckoff position: the center, horizontal and vertical coordinate axes, diagonal axes, and general position (denoted by white space).

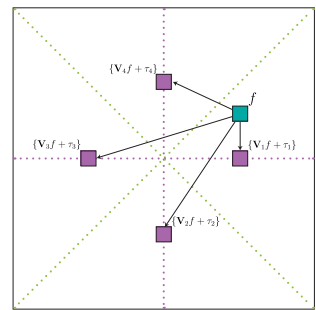


Figure 3: Projection of a coordinate  $f$  using Wyckoff position  $w$ .

162 **Flow Matching (FM)** is a generative modeling framework that transform samples from a simple  
 163 base distribution  $p_0$  into a complex target distribution  $p_1$  using a time-dependent diffeomorphic  
 164 map, called a flow,  $\psi : [0, 1] \times \mathcal{X} \rightarrow \mathcal{X}$ . This flow is defined through the differential equation:  
 165

$$166 \quad \frac{d}{dt} \psi_t(x) = v_t(\psi_t(x)), \quad \psi_0(x) = x \quad (2)$$

168 where  $v_t : [0, 1] \times \mathcal{X} \rightarrow \mathcal{X}$  is a vector field governs the evolution of the  $\psi_t$ . The flow induces a  
 169 time-dependent probability density path  $p_t : [0, 1] \times \mathcal{X} \rightarrow \mathbb{R}$  starting at  $p_0$  and ending with  $p_1$ .  
 170 FM trains a parametric approximation  $u_t$  of the true vector field  $v_t$  (Lipman et al., 2024) by solving  
 171 a regression objective. A conditional flow  $\psi(\cdot | y) : [0, 1] \times \mathcal{X} \rightarrow \mathcal{X}$  transports the entire base  
 172 distribution to a single target point  $y \in \mathcal{X}$  and is governed by vector field  $v_t(\cdot | y)$ , which is easy to  
 173 compute, unlike  $v_t(\cdot)$ . Lipman et al. (2022) demonstrated that optimizing  $u_t$  to match  $v_t(\cdot | y)$  with  
 174 regression leads to the same optimum as matching the marginal vector field  $v_t$ .  
 175

### 176 3 METHOD

178 This section presents our proposed model, SGFM, a flow matching-based generative approach de-  
 179 signed to sample crystal structures conditioned on specified space groups and Wyckoff positions.  
 180 We start by formalizing the problem and defining the target distribution we aim to sample from in  
 181 section 3.1. Then, section 3.2 outlines sufficient conditions for a flow model to sample from this  
 182 distribution. Section 3.3 provides a detailed overview of the model, including its key components,  
 183 the noise prior and vector field. Finally, section 3.4 presents the training details of SGFM.  
 184

#### 185 3.1 PROBLEM DEFINITION

186 Given a finite set of crystals  $\{c_1, \dots, c_m\}$ , each associated with a space group and Wyckoff posi-  
 187 tions  $(G_i, \mathcal{W}_i)$  and drawn from an unknown target distribution  $q$ , our goal is to design a generative  
 188 model that samples crystals  $c \sim p_1$  such that  $p_1 \approx q$ . To incorporate the structural information  
 189 encoded by  $G$  and  $\mathcal{W}$ , we factorize the distribution as  $p_1(c) = p_1(c | G, \mathcal{W})q(G, \mathcal{W})$ , enabling us  
 190 to model the crystal distribution conditionally on  $G$  and  $\mathcal{W}$ . While  $G$  and  $\mathcal{W}$  are jointly sampled  
 191 from empirical distribution, the proposed generative model focuses on sampling crystals from the  
 192 conditional distribution  $c \sim p_1(\cdot | G, \mathcal{W})$ , which satisfies the following properties:  
 193

- 194 •  $p(\cdot | G, \mathcal{W})$  is a *G-symmetric* distribution, meaning that  $p(c | G, \mathcal{W}) > 0$  if  $c$  is *G-*  
 195 *symmetric*. The distribution assigns positive probability exclusively to crystals for which  
 196  $G$  is their corresponding space group.
- 197 •  $p(\cdot | G, \mathcal{W})$  is a *W-constructable* distribution, meaning that  $p(c | G, \mathcal{W}) > 0$  if  $c$  is *W-*  
 198 *constructable*.  $p$  only supports crystals with fractional coordinates constructible by  $\mathcal{W}$ .

199 While the definitions provide a full description of the required distribution, they can be further sim-  
 200 plified. The following lemma shows that, given  $G$  and  $\mathcal{W}$ , where  $\mathcal{W}$  denotes the Wyckoff positions  
 201 associated with the space group  $G$ , a  $\mathcal{W}$ -constructable distribution implies a *G-symmetric* distribu-  
 202 tion.  
 203

204 **Lemma 3.1.** *Let  $G \leqslant E(3)$  be a space group,  $\mathcal{W}$  a corresponding set of Wyckoff positions and*  
 205  *$F \in [0, 1]^{n \times 3}$  a  $\mathcal{W}$ -constructable set of points in the unit cell, then  $F$  is *G-symmetric*.*

206 The proof (appendix A.3) relies on the fact that the action of a group element on an orbit defines a  
 207 bijection.  
 208

#### 209 3.2 THEORETICAL ANALYSIS

211 We now present the theoretical concepts underpinning the development of our generative model.  
 212 The following theorem establishes the conditions under which a flow-based model can sample from  
 213 a *G-invariant* distribution. This result has been proven in prior work by Köhler et al. (2020); Rezende  
 214 et al. (2019); Song et al. (2023). For completeness, we state the theorem here and provide a concise  
 215 version of its proof in appendix A.1, as it serves as a foundational component for our theoretical  
 analysis.

216 **Algorithm 1** Sample  $\mathbf{F}_0 \sim p_0(\cdot | G, \mathcal{W})$ 


---

```

217 1: Input:  $\mathcal{W} = \{w_1, \dots, w_k\}$  s.t.  $w_i$  is a Wyckoff position of the space group  $G$ .
218 2: Output:  $\mathbf{F}_0 \in [0, 1]^{n \times 3}$  s.t.  $n = \sum_{i=1}^k |w_i|$ .
219 3: set  $\mathbf{F}_0 = []$ 
220 4: for  $i = 1$  to  $k$  do
221 5:   Sample  $x \sim \mathcal{U}[0, 1]^3$ 
222 6:    $\mathbf{F}_0 = \text{Concatenate}([\mathbf{F}_0, w_i(x)])$ 
223 7: end for
224 8: return  $\mathbf{F}_0$ 
225
226

```

---

227 **Theorem 3.2.** *The probability path  $p_t(x)$  defined by a flow generated by a  $G$ -equivariant vector  
228 field  $u_t$  from a  $G$ -invariant prior  $p$  is  $G$ -invariant for all  $t \in [0, 1]$ .*

230 The proof of this theorem consists of two parts. First, we demonstrate that the flow  $\psi_t(x)$ , is  $G$ -  
231 equivariant. Second, we show  $p_t(x)$  is  $G$ -invariant. Building on this proof, we derive the conditions  
232 under which a flow-based model can sample from a distribution that is  $\mathcal{W}$ -constructable. Achieving  
233 this requires extending the standard framework with two modifications:

234 1. Introducing a noise prior that is itself  $\mathcal{W}$ -constructable.  
235 2. Ensuring that the vector field model  $u_t$  is equivariant with respect to the space group  $G$  and  
236 the permutation group  $S_n$ . To do so we extend the vector field (and corresponding flow)  
237 equivariance to the group product  $G \times S_n$ .

239 **Theorem 3.3.** *The probability path  $p_t(x)$  defined by a flow generated by a  $G \times S_n$  equivariant  
240 vector field  $u_t$  from a  $\mathcal{W}$ -constructable prior  $p$  is  $\mathcal{W}$ -constructable for all  $t \in [0, 1]$ .*

241 This theorem follows directly from the lemma below (proof in appendix A.2), which establishes  
242 that if the initial point  $c_0$  of a  $G \times S_n$  equivariant flow is a  $G$ -symmetric crystal structure, any  
243 point along the flow will be mutually  $G$ -symmetric with  $c_0$ . **Based on the mutual  $G$ -symmetry**,  
244 we demonstrate that the flow preserves the site-symmetry structure of  $c_0$ . This implies that if  $c_0$  is  
245  $\mathcal{W}$ -constructable, then  $\psi_t(c_0)$  is also  $\mathcal{W}$ -constructable. Figure 1 (b) visualizes the core idea behind  
246 the theorem, illustrating how the equivariant vector field constrains atoms to move solely within the  
247 image of their Wyckoff position.

248 **Lemma 3.4.** *Let  $\psi_t$  be a  $G \times S_n$  equivariant flow and  $c \in \mathcal{C}$  be  $G$ -symmetric and  $\mathcal{W}$ -constructable,  
249 then  $\psi_t(c)$  is  $G$ -symmetric and  $\mathcal{W}$ -constructable.*

## 251 3.3 SGFM

253 In this section, we introduce the key components of SGFM, with emphasis on the prior model and the  
254 learned vector field architecture. We explain how the previously outlined conditions are concretely  
255 implemented. The main focus lies in the interaction between the method and the crystal's fractional  
256 coordinates, due to their strong dependence on the space group and Wyckoff positions.

257 **Noise Prior.** According to theorem 3.3, for the generated distribution to satisfy the conditions  
258 outlined in section 3.1, the noise prior must also satisfy the same constraints. Algorithm 1 presents a  
259 noise prior sampling pseudocode (with 2D visualizations in fig. 1 (a)) that generates initial fractional  
260 coordinates compliant with these requirements. The sampling procedure for the lattice parameters  
261 and atom types is described in section 3.4 for the reader's convenience. The algorithm iterates over  
262 the set of Wyckoff positions and samples orbits induced by  $G$  by projecting random points from the  
263 unit cell. It follows directly from the algorithm's construction that  $\mathbf{F}_0$  is  $\mathcal{W}$ -constructable (and also  
264  $G$ -symmetric).

265 **Space Group Conditional Vector Field.** As noted previously,  $u_t$  must be  $G \times S_n$  equivariant in  
266 order for the flow to be  $G$ -symmetric and  $\mathcal{W}$ -constructable. The challenge lies in using a single  $u_t$   
267 model across crystals with varying space groups. Since some space groups (with non-orthogonal  
268 lattice structure) act on the fractional coordinates with special affine structured transformations, (see  
269 fig. 5), using an  $E(3) \times S_n$ -equivariant model is non-trivial. **In addition, modeling  $G$ -equivariance  
using a super group restricts the expressiveness of the model.** To address these limitations, we adopt

270 Group Averaging (GA) (Yarotsky, 2022), a symmetrization operator that projects a backbone model  
 271 onto the space of  $G$ -equivariant functions. It is defined as:

$$273 \quad \hat{u}(c | G) = \frac{1}{|G|} \sum_{g \in G} g \cdot u(g^{-1} \cdot c). \quad (3)$$

275 Applying GA to enforce space group symmetry addresses the previously mentioned limitations.  
 276 Specifically, if the backbone  $u$  is  $S_n$  equivariant, then  $\hat{u}(\cdot | G)$  is  $G \times S_n$  equivariant (Puny et al.,  
 277 2021). Additionally, GA is not limited to subgroups of  $E(3)$  and support all finite groups. Import-  
 278 antly, Puny et al. (2021) showed that symmetrization preserves the expressive power of the original  
 279 model. However, a drawback of GA is its computational burden: directly applying eq. (3) increases  
 280 the number of evaluations of  $u$  by a factor of  $|G|$ , which can be as large as 192 for 3D space groups  
 281 (the average space group size in the MP-20 dataset is  $\sim 45$ ). To mitigate this computationally inten-  
 282 sive formulation, we leverage the fact that the inputs to  $\hat{u}(\cdot | G)$  are  $G$ -symmetric crystals, allowing  
 283 us to derive an efficient and equivalent formulation of GA specific to this case.

284 **Lemma 3.5.** *Let  $c \in \mathcal{C}$  be a crystal,  $G$  its space group, and  $u$  an  $S_n$  equivariant vector field. Then,  
 285 eq. (3) can be equivalently rewritten as follows:*

$$286 \quad \hat{u}(c | G) = \frac{1}{|G|} \sum_{g \in G} g \cdot \sigma_{g^{-1}|c} \cdot u(c) \quad (4)$$

288 Where  $\sigma_{g^{-1}|c} \in S_n$  satisfy the equation  $\sigma_{g^{-1}|c} \cdot c = g^{-1} \cdot c$ .

290 The formulation presented in eq. (4) requires only a single  
 291 evaluation of  $u$ , which dramatically improves the model ef-  
 292 ficiency. Figure 1 (c) compares between eq. (3) and eq. (4)  
 293 and visualize the efficiency gain. Furthermore, computing  
 294  $\sigma_{g^{-1}|c}$  is computationally efficient, since we can decompose  
 295 the problem according to the orbits of  $c$ , determined by  $\mathcal{W}$  (ap-  
 296 pendix A.3). At inference time, these permutations only need  
 297 to be computed once for  $c_0$ , since theorem 3.3 guarantees that the flow preserves  $G$ -symmetry struc-  
 298 ture. During training, permutations are computed only once during preprocessing for every data  
 299 point. Table 1 compares the training and generation runtimes between SGFM, a non-equivariant  
 300 variant (no symmetrization), and standard GA highlighting the efficiency gains of our GA implemen-  
 301 tation compared to the standard GA, and demonstrating that its computational cost is comparable to  
 302 using a backbone without symmetrization. Further details of this comparison are in appendix H.

### 303 3.4 TRAINING SGFM

305 This section provides an overview of the SGFM training process. Let  $c_1 \in \mathcal{C}$  be a crystal from  
 306 the training set with a corresponding space group  $G$  and Wyckoff positions  $\mathcal{W}$ . We will denote  
 307  $c_0 \sim p_0(\cdot | G, \mathcal{W}, c_1)$  a sample from the conditional noise prior,  $c_t = \psi_t(c_0 | c_1)$  the conditional flow  
 308 where  $c_t = (k_t, \mathbf{F}_t, \mathbf{A}_t)$ ,  $v_t(c_t | c_1) = (v_t^k(c_t | c_1), v_t^F(c_t | c_1), v_t^A(c_t | c_1))$  is the conditional vector  
 309 field and  $\hat{u}_t(c_t | G) = (\hat{u}_t^k(c_t | G), \hat{u}_t^F(c_t | G), \hat{u}_t^A(c_t | G))$  is the prediction of the  $G \times S_n$  equivariant  
 310 vector field parametric model.

311 **Lattice Parameters.** As noted in section 2, we represent lattice parameters using the group-  
 312 conditioned form from (Jiao et al., 2024), where  $k \in \mathbb{R}^6$  encodes the basis coefficients of a 3D  
 313 symmetric matrix constrained to  $G$ -specific subspaces. To sample  $k_0 \in \mathbb{R}^6$ , we first draw coeffi-  
 314 cients  $k' \sim \mathcal{N}(0, \mathbf{I})$  and apply a group condition mask:  $k_0 = k' \odot m(G)$ , where  $m(G) \in \{0, 1\}^6$  is  
 315 a group-dependent binary mask that zeros out the irrelevant coefficients. For hexagonal lattices we  
 316 set the first entry of  $k_0$  to be  $\frac{-\log(3)}{4}$ , as described in table 5  $k_t$  is computed as a linear interpolation  
 317 of  $k_0$  and  $k_1$ ,  $k_t = (1 - t)k_0 + tk_1$  and the corresponding component of the conditional vector field  
 318 is  $v_t^k(c_t | c_1) = k_1 - k_0$ . Since the group action does not directly act on the lattice parameterization  
 319 we need to apply the  $m(G)$  on  $\hat{u}_t^k(c_t | G)$ , both in training and after each generation step. The lattice  
 320 optimization objective is:

$$321 \quad \mathcal{L}^k(\theta) = \mathbb{E}_{t, q(c_1), p_0(c_0 | G)} \left\| \hat{u}_t^k(c_t | G) \odot m(G) - (k_1 - k_0) \right\|_2^2 \quad (5)$$

323 **Atom Types.** For the DNG task, which involves predicting atom types, we follow the model-  
 324 ing approach introduced in Miller et al. (2024), where atom types are represented using a  $\{-1, 1\}$

Table 1: Training and generation time comparison of different vector field models.

Model	Training		Generation Time (s)
	Batch size	Time (s)	
SGFM	64	28.2	17.81
Non-Equivariant	64	26.3	16.39
GA	1	600	14.2

binary format instead of standard one-hot encoding. Specifically,  $A_1 \in \{0, 1\}^{n \times h}$  is converted into its binary representation  $\tilde{A}_1 \in \{-1, 1\}^{n \times \lceil \log_2 h \rceil}$ . To ensure  $G$ -symmetry in the initial sample  $c_0$ , atom types must be consistent within each orbit. Accordingly, we sample initial Gaussian noise  $\mathcal{N}(0, 1)^{\lceil \log_2 h \rceil}$  per orbit and broadcast it to all atoms within that orbit to sample  $\tilde{A}_0 \in \{-1, 1\}^{n \times \lceil \log_2 h \rceil}$ . We define  $\tilde{A}_t = (1 - t)\tilde{A}_0 + t\tilde{A}_1$  and  $v_t^A(c_t|c_1) = \tilde{A}_1 - \tilde{A}_0$ . The atom types optimization objective is:

$$\mathcal{L}^A(\theta) = \mathbb{E}_{t, q(c_1), p_0(c_0|G)} \left\| \hat{u}_t^A(c_t|G) - (\tilde{A}_1 - \tilde{A}_0) \right\|_2^2 \quad (6)$$

Our GA formulation (eq. (4)) ensures that  $\hat{u}_t^A(c_t | G)$  is  $G$ -invariant, meaning the atom type vector field is consistent across orbits, as required. [Detailed explanation about this property can be found in appendix G.3](#). During inference, we apply the sign function to convert the continuous atom type predictions into their binary representation.

**Fractional Coordinates.** Algorithm 1 describes a general procedure for sampling fractional coordinates that are both  $G$ -symmetric and  $\mathcal{W}$ -constructable. To ensure  $G$ -symmetry of the conditional flow, the initial coordinates  $\mathbf{F}_0 \sim p_0(\cdot, |, G, \mathcal{W})$  must be  $G$ -symmetric with  $\mathbf{F}_1$ . This requires that the order of elements and operators in  $\mathcal{W}$  match that used to generate  $\mathbf{F}_1$ , which we precompute during preprocessing using the PyXtal library (Fredericks et al., 2021). We adopt the flat torus geometry of the unit cell, following the approach proposed by Miller et al. (2024), and define the conditional flow over the fractional coordinates,

$$\psi_t(\mathbf{F}_0|\mathbf{F}_1) = \mathbf{F}_0 + t \cdot \log_{\mathbf{F}_0}(\mathbf{F}_1), \quad (7)$$

$$\log_{\mathbf{F}_0}(\mathbf{F}_1) = \frac{1}{2\pi} \text{atan2}([\sin(\mathbf{F}_1 - \mathbf{F}_0), \cos(\mathbf{F}_1 - \mathbf{F}_0)]). \quad (8)$$

Where  $\log(\cdot)(\cdot)$  is the element-wise logarithmic map over the flat tori. In appendix B we demonstrate: (1) the conditional vector field  $\log_{\mathbf{F}_0}(\mathbf{F}_1)$  is  $G$ -equivariant but with respect to a different representation of  $G$ . Let  $g \in G$  then  $\log_{g \cdot \mathbf{F}_0}(g \cdot \mathbf{F}_1) = g^* \log_{\mathbf{F}_0}(\mathbf{F}_1)$  where  $g^*$  is defined by the homomorphism  $(\mathbf{R}, \tau) \mapsto \mathbf{R}$ ; (2)  $\psi_t(\mathbf{F}_0|\mathbf{F}_1)$  is mutually  $G$ -symmetric with  $\mathbf{F}_0$  and  $\mathbf{F}_1$ , hence  $G$ -symmetric and  $\mathcal{W}$ -constructable. The fractional coordinates optimization objective is:

$$\mathcal{L}^F(\theta) = \mathbb{E}_{t, q(c_1), p_0(c_0|G, \mathcal{W})} \left\| \hat{u}_t^F(c_t|G) - \log_{\mathbf{F}_0}(\mathbf{F}_1) \right\|_2^2 \quad (9)$$

Combining all components and hyperparameters  $\lambda_k, \lambda_F, \lambda_A \in \mathbb{R}^+$  we obtain our training objective:

$$\mathcal{L}^{\text{SGFM}}(\theta) = \lambda_k \mathcal{L}^k(\theta) + \lambda_F \mathcal{L}^F(\theta) + \lambda_A \mathcal{L}^A(\theta). \quad (10)$$

## 4 EXPERIMENTS

The experiments can be divided into two sections: *Crystal Structure Prediction* (CSP) implies predicting the fractional coordinates and lattice parameters given atom types and number of atoms in the unit cell. In practical CSP tasks in materials science the atom types and the number of atoms in the unit cell is unknown, but our CSP benchmark remains a useful unit test nevertheless. In this task, knowledge of the correct Wyckoff positions provides a significant advantage. We therefore differentiate DiffCSP++ and SGFM from the other models in this experiment, but provide evaluations of models without this knowledge for completeness. Since our contribution is primarily about effectively conditioning on space groups and Wyckoff positions, the most important comparison is between models that have access to the ground truth wyckoff positions. This unit test evaluation removes the ambiguity of inaccurate Wyckoff positions for matching to ground truth structures. We also provide results using a method where the Wyckoff positions are inferred using a heuristic method (Kusaba et al., 2022). We test on five datasets and perform ablation studies to assess our method.

In the second task *De Novo Generation* (DNG), we generate the atom types along with the fractional coordinates and lattice parameters to accurately simulate a computational materials discovery campaign. We evaluate models based upon the number of thermodynamically stable, unique, and novel (S.U.N.) structures they generate. We consider two instantiations of our model: SGFM when we use the empirical distribution (training data) to provide Wyckoff positions and the setting where a model proposed Wyckoff positions (Kazeev et al., 2025). We train on the experimental MP-20 dataset.

378 **Datasets.** We evaluate our method on five datasets: *MP*-20 (Jain et al., 2013), with 45,231 diverse  
 379 crystals from the Materials Project; *MPTS*-52, a time-ordered variant with 40,476 crystals featuring  
 380 larger unit cells; and *Alex-MP*-20, a large-scale set of 607,684 crystals combining *MP*-20 and  
 381 Alexandria data (Schmidt et al., 2022a;b). We also assess CSP on two unit-test style datasets: *Perov*-  
 382 5 (Castelli et al., 2012), with 18,928 perovskites sharing a common structure but varying atom types,  
 383 and *Carbon*-24 (Pickard, 2020), containing 10,153 carbon crystals with diverse structures.

384 **Baselines.** We compared SGFM to several state-of-the-art baselines. Methods that do not incorpo-  
 385 rate space group information in their generation process include *CDVAE* (Xie et al., 2021), *ADiT*  
 386 (Joshi et al., 2025), *FlowMM* (Miller et al., 2024), *FlowLLM*, *MatterGen* (Zeni et al., 2023), *Dif-  
 387 FCSP* (Jiao et al., 2023), (Sriram et al., 2024), and *OMatG* (Hoellmer et al., 2025). In contrast,  
 388 *SymmCD* (Levy et al., 2025), *DiffCSP++* (Jiao et al., 2024), *WyFormer* (Kazeev et al., 2025), and  
 389 *SGEquiDiff* (Chang et al., 2025) explicitly incorporate space group information. Additional details  
 390 on each baseline are provided in appendix C.

391 **Model Details.** To model  $\hat{u}_t$ , we adopt the architecture used in Miller et al. (2024), which utilizes  
 392 *EGNN* (Satorras et al., 2022) to handle fractional coordinates. The model applies sinusoidal embed-  
 393 dings to the fractional coordinates, ensuring invariance to lattice translations in addition to the space  
 394 group equivariance. A description of the architecture and the hyperparameters used in each experi-  
 395 ment are provided in appendix G. For improved sampling quality, we apply inference anti-annealing  
 396 (Yim et al., 2023; Bose et al., 2023) that adjusts the prediction velocity during generation.

397 Table 2: Crystal Structure Prediction. MR denotes match rate. *uniform* implies a uniform base  
 398 distribution, *GA* denotes group average. Best results are in bold within groupings regarding access  
 399 to explicit Wyckoff positions. Access categories are {None, Predict with CSPML, Ground truth}.  
 400 (we will fill in missing RMSE values, there is a logistical issue in getting them at the moment)

Model	Wyckoff Positions	MP-20		MPTS-52		Perov-5		Carbon-24		Alex-MP-20	
		MR (%) ↑	RMSE ↓	MR (%) ↑	RMSE ↓						
CDVAE		33.90	.1045	5.34	.2106	45.31	.1138	17.09	.2969	-	-
DiffCSP		51.49	0.0631	12.19	0.1786	52.02	0.0760	17.54	<b>0.2759</b>	-	-
FlowMM	None	61.39	<b>.0566</b>	17.54	<b>.1726</b>	53.15	<b>.0992</b>	<b>23.47</b>	.4122	-	-
OMatG		<b>69.83</b>	.0741	<b>27.38</b>	.1970	<b>83.06</b>	.3753	-	-	72.50	.1260
SGFM (uniform)		64.49	-	-	-	-	-	-	-	-	-
CSPML	Predict	70.51	-	36.98	-	51.84	-	-	-	-	-
DiffCSP++	with	<b>70.58</b>	.0272	<b>37.17</b>	.0676	52.17	.0841	-	-	-	-
SGFM	CSPML	70.13	-	35.09	-	<b>54.10</b>	-	-	-	-	-
DiffCSP++	Ground	80.27	.0295	46.29	.0896	98.44	.0430	-	-	83.18	<b>.0188</b>
SGFM (no GA)	truth	68.16	-	-	-	-	-	-	-	-	-
SGFM		<b>82.74</b>	<b>.0288</b>	<b>51.79</b>	<b>.0827</b>	<b>98.57</b>	<b>.0188</b>	<b>55.02</b>	<b>.0952</b>	<b>84.40</b>	.0198

## 413 CRYSTAL STRUCTURE PREDICTION

414 The generative task in CSP requires sampling from the conditional target distribution  $c \sim q(\cdot | \mathbf{A})$ ,  
 415 where  $\mathbf{A}$  denotes a predefined atom type composition. This conditioning implies that during both  
 416 training and generation  $A_t = \mathbf{A}$  for all  $t \in [0, 1]$ , effectively ignoring the loss term  $\mathcal{L}^A$  and the  
 417 atom type component  $\hat{u}_t^A(c_t | G)$ . For evaluation, a crystal structure is generated for each entry in  
 418 the test set and then compared against the corresponding ground truth structure using pymatgen  
 419 *StructureMatcher* (Ong et al., 2013) with same threshold values as in Jiao et al. (2024). We  
 420 report two metrics: the match rate (MR), defined as the fraction of generated structures that suc-  
 421 cessfully match their ground truth counterparts, and the RMSE, averaged over all matched pairs. We  
 422 conduct CSP on all datasets and with multiple ablations that we explain below. Results in table 2.

423 **Ground truth Wyckoff positions (with efficient Group Averaging)** In this section we quantify  
 424 CSP performance among models that access the ground truth Wyckoff positions. We determine  
 425 how well each algorithm can utilize this useful, but in-practice unobserved, information. We com-  
 426 pare our model SGFM, with and without (*no GA*) the efficient group average, to the only baseline  
 427 method that performs this task: DiffCSP++. In this setting, SGFM outperforms others across all  
 428 datasets achieving state-of-the-art results on every metric except Alex-MP-20 RMSE. Comparing  
 429 CSP accuracy as a function of generation steps (fig. 4), we observe that SGFM reaches near-optimal  
 430 accuracy within just 50–100 steps. DiffCSP++ converges more slowly, requiring up to 1000 steps to  
 431 approach its best performance—while still showing a notable gap in match rate compared to SGFM.

432 This difference is likely due to SGFM’s flow matching formulation. In this same plot, we include a  
 433 version of SGFM without anti-annealing to assess the effects of anti-annealing on performance.  
 434

435 We include SGFM (no GA) without the group average as an  
 436 ablation study. The model remains conditional on ground truth  
 437 Wyckoff positions because the prior depends on them; how-  
 438 ever, the vector field is not conditional nor equivariant with  
 439 respect to  $G$ . Performance degrades by a significant factor.

440 **Predicting Wyckoff positions with CSPML** Now that we  
 441 know conditioning on the ground truth Wyckoff positions can  
 442 produce such strong results, how can apply our method with  
 443 the Wyckoff positions are unknown? We utilize *CSPML* (Kus-  
 444 ababa et al., 2022), a metric learning-based model that, given an  
 445 atom type composition, retrieves a similar composition from a  
 446 template set—along with its associated space group and Wyck-  
 447 off positions. We then use those Wyckoff positions as input to  
 448 SGFM and DiffCSP++ to perform the benchmark. The dif-  
 449 ferences between CSPML, which also includes a method for  
 450 predicting atomic coordinates; DiffCSP++; and SGFM are rel-  
 451 atively minor according to table 2. We take this result as ev-  
 452 idence that correctly guessing the Wyckoff positions is an ex-  
 453 tremely important step in accurately performing the CSP unit  
 454 test. Methods that directly predict atomic coordinates outper-  
 455 form the CSPML-conditional results, implying that there is  
 456 room for innovation in predicting Wyckoff positions.

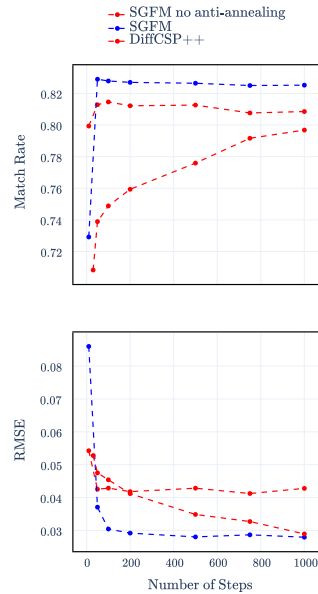
457 **Results without Wyckoff positions** We completely ablate the space group conditional aspects of  
 458 our model and apply it without the group average and without the Wyckoff position conditional  
 459 prior, replacing it with a uniform prior on atomic coordinates. SGFM (uniform) becomes a test  
 460 of the architecture itself. Performance is competitive with OMatG on MP-20. Considering all the  
 461 ablations and comparing to models that have access to ground truth Wyckoff positions, the gap  
 462 between SGFM (uniform) and SGFM (no GA) is smaller than between SGFM (no GA) and SGFM.  
 463 This comparison quantifies the value of a Wyckoff conditional prior compared to the group average.

464  
 465 **Table 3: DNG evaluation.** Models were trained on the MP-20 dataset. NFE refers to the number  
 466 of generation steps per sample. We evaluated all the S.U.N. metrics, except those marked with \*.  
 467 Methods above the dividing line do not explicitly use Wyckoff positions; methods below use them.

Model	NFE	Validity (%) $\uparrow$		$d_\rho$	$d_{\text{elem}}$	$d_{\text{cn}}$	Stable (%) $\uparrow$ S.U.N (%) $\uparrow$		Stable (%) $\uparrow$ S.U.N (%) $\uparrow$	
		Structural	Composition				$E_{\text{hull}} < 100 \text{ meV/Atom}$	$E_{\text{hull}} < 0 \text{ meV/Atom}$	$E_{\text{hull}} < 0 \text{ meV/Atom}$	$E_{\text{hull}} < 0 \text{ meV/Atom}$
CDVAE	5000	<b>100.00</b>	86.70	0.688	0.278	-	-	-	-	-
ADiT	500	99.74	<b>92.14</b>	-	-	-	<b>72.0</b>	27.4	13.0	4.6
FlowMM	500	96.86	83.24	0.075	0.079	0.443	31.2	19.7	4.6	2.3
FlowLLM	250	99.81	89.05	0.660	0.090	-	67.9	21.9	14.2	3.6
MatterGen	1000	100.00	82.60	0.206	0.242	-	-	24.3	-	-
OMatG	680	95.05	82.84	<b>0.060</b>	<b>0.017</b>	0.165	44.4	23.7	6.6	2.2
SymmCD	1000	90.34	85.81	0.230	0.400	-	-	-	-	-
DiffCSP++ (empirical)	1000	99.94	85.12	0.235	0.374	-	31.4	21.1	7.2	4.0
DiffCSP++ (Wyformer)	1000	99.66	80.34	0.670	0.098	-	-	-	-	3.8*
SGEquiDiff	1000	99.25	86.16	0.193	0.209	-	-	25.8*	-	-
SGFM (empirical)	500	99.87	86.81	0.075	0.181	<b>0.076</b>	64.1	<b>30.3</b>	<b>14.6</b>	<b>6.9</b>
SGFM (Wyformer)	500	99.87	84.76	0.237	0.233	-	48.4	22.6	10.6	4.7

## 480 DE NOVO GENERATION

481 We evaluate the ability of our generative model to discover thermodynamically stable, unique, and  
 482 novel crystals; identify the validity of the generated samples; and investigate divergences between  
 483 property distributions. Novel structures do *not* appear in the training or validation splits of MP-20.  
 484 Results and baselines are shown in table 3. SGFM conditioned on empirical Wyckoff positions  
 485 produces SOTA results overall. SGFM using Wyformer is SOTA at the tighter stability threshold.



486 Figure 4: MR ( $\uparrow$ ) and RMSE ( $\downarrow$ )  
 487 versus integration steps on MP-20.

486 These are the evaluation metrics: *Validity* % defines two different  
 487 heuristics that realistic crystals should satisfy. *Structural validity*  
 488 implies that the pairwise atomic distances of a crystal’s atoms are  
 489 all greater than 0.5Å. *Compositional validity* implies that a crystal  
 490 has a neutral charge according to so-called SMACT (Davies et al.,  
 491 2019) rules. The *properties* that we consider for computing diver-  
 492 gences include  $\rho$  the atomic density defined by number of atoms  
 493 divided by unit cell volume,  $\text{elem}$  (airity) the number of unique ele-  
 494 ments in a crystal, and  $\text{cn}$  (coordination number) or the the number  
 495 of bonds per atom on average. We report the Wasserstein divergence between the test set and a  
 496 structurally and compositionally valid subset of 1000 generated samples. Finally, we compute the  
 497 *thermodynamic stability*, *novelty*, and *uniqueness* of generated crystals. Thermodynamic stability  
 498 implies a structure is at or near a local minima in composition space. This requires a short ex-  
 499 planation which can be read in appendix D. We then compute the uniqueness and novelty of each  
 500 stable crystal (*S.U.N.*) against other generations and the train and validation set, respectively using  
 501 StructureMatcher (Ong et al., 2013) with default settings.

502 We trained SGFM on the MP-20 dataset, including an atom type prediction module, and generated  
 503 structures from each of our configurations for evaluation. The configurations include using Wyckoff  
 504 positions taken from the train set, denoted *empirical*, and from the output of *Wyformer* (Kazeev et al.,  
 505 2025), with an eponymous denotation. All systems were evaluated with 10, 000 samples, except  
 506 DiffCSP++ (*empirical*) that uses only 1, 000 samples. DiffCSP++ (*Wyformer*) (Kazeev et al., 2025)  
 507 and SGEquiDiff (Chang et al., 2025) are reported results with slightly different density functional  
 508 theory settings and only 100 relaxations, respectively. **To further assess the generation efficiency of**  
 509 **SGFM relative to other models, we measured generation times (across multiple batch sizes) on a**  
 510 **single NVIDIA L40S GPU. The results are reported in table 4. Despite requiring more parameters**  
 511 **(16.2M compared to 12.2M for DiffCSP++ and 5.5M for SGEquiDiff) and operating on the full unit**  
 512 **cell rather than the asymmetric unit (which is more memory-efficient), SGFM achieves comparable**  
 513 **efficiency to SGEquiDiff and outperforms DiffCSP++.**

## 5 RELATED WORK

514 There is a growing body of literature about generative models for inorganic crystals. We focus here  
 515 on works with similar inductive biases, namely explicit utilization of Wyckoff positions. We first  
 516 consider works that generate atomic coordinates. Cao et al. (2024) created an autoregressive model  
 517 that generates crystals sequentially in Wyckoff position’s lexicographic order. Jiao et al. (2024);  
 518 Levy et al. (2025) produced diffusion models that both represent crystals within the asymmetric  
 519 unit, a memory-efficient formulation that contains just one representative per orbit. Neither of these  
 520 methods utilize space group equivariance and both require projection steps to keep atomic coordi-  
 521 nates within the target Wyckoff positions. A concurrently developed diffusion model by Chang et al.  
 522 (2025) also utilizes the asymmetric unit; however, it implements space group equivariance via group  
 523 averaging and does not require projection. Working in the asymmetric unit does not allow for our  
 524 efficient reformulation in eq. (4) **since representing the crystal structure through the asymmetric unit**  
 525 **does not yield a  $G$ -symmetric representation.** As written, Levy et al. (2025) do not address the crystal  
 526 structure prediction problem. There are also a class of models that generate coarse-grained Wyck-  
 527 off positions alone, ignoring explicit atomic coordinates. (Zhu et al., 2024; Kazeev et al., 2025;  
 528 Kelvinius et al., 2025) both take this approach, inspired by regression methods (Goodall & Lee,  
 529 2020; Goodall et al., 2022). These models synergize with ours and can generate Wyckoff positions  
 530 for SGFM to use in DNG in section 4. Innovations in these methods, if conditional on atom types,  
 531 could replace CSPML for CSP. Further discussion of other relevant work is left for appendix E.

## 6 CONCLUSIONS

532 In this work, we introduced SGFM, a FM based generative model for crystal structures, conditioned  
 533 on space group and Wyckoff positions. By design, SGFM produces crystals that satisfy symmetry  
 534 constraints, relying on sufficient conditions we formulated over the noise prior and vector field. We  
 535 also implemented an efficient group averaging method, enabling the incorporation of space group  
 536 equivariance into the vector field model with minimal overhead. Evaluated on both CSP and DNG

Table 4: Generation times for various batch sizes.

Model	Generation Time			
	(s/batch)	64	256	500
DiffCSP++	66	268	490	
SGEquiDiff	19	75	154	
SGFM	22	92	175	

540 tasks, SGFM achieved state-of-the-art performance. Future directions include extending the model  
 541 to an unconditional generation setting, where space group and Wyckoff positions are also generated  
 542 rather than specified.

543

544

## 545 REFERENCES

546 Michael S Albergo and Eric Vanden-Eijnden. Building normalizing flows with stochastic inter-  
 547 polants. *arXiv preprint arXiv:2209.15571*, 2022.

548

549 Michael S. Albergo, Nicholas M. Boffi, and Eric Vanden-Eijnden. Stochastic interpolants: A uni-  
 550 fying framework for flows and diffusions, 2023. URL <https://arxiv.org/abs/2303.08797>.

551

552 Luis Barroso-Luque, Muhammed Shuaibi, Xiang Fu, Brandon M Wood, Misko Dzamba, Meng  
 553 Gao, Ammar Rizvi, C Lawrence Zitnick, and Zachary W Ulissi. Open materials 2024 (omat24)  
 554 inorganic materials dataset and models. *arXiv preprint arXiv:2410.12771*, 2024.

555

556 Avishek Joey Bose, Tara Akhoud-Sadegh, Kilian Fatras, Guillaume Huguet, Jarrid Rector-Brooks,  
 557 Cheng-Hao Liu, Andrei Cristian Nica, Maksym Korablyov, Michael Bronstein, and Alexan-  
 558 der Tong. Se (3)-stochastic flow matching for protein backbone generation. *arXiv preprint*  
 559 *arXiv:2310.02391*, 2023.

560

561 Zhendong Cao, Xiaoshan Luo, Jian Lv, and Lei Wang. Space group informed transformer for  
 562 crystalline materials generation, 2024. URL <https://arxiv.org/abs/2403.15734>.

563

564 Ivano E Castelli, David D Landis, Kristian S Thygesen, Søren Dahl, Ib Chorkendorff, Thomas F  
 565 Jaramillo, and Karsten W Jacobsen. New cubic perovskites for one-and two-photon water splitting  
 566 using the computational materials repository. *Energy & Environmental Science*, 5(10):9034–  
 9043, 2012.

567

568 Rees Chang, Angela Pak, Alex Guerra, Ni Zhan, Nick Richardson, Elif Ertekin, and Ryan P Adams.  
 569 Space group equivariant crystal diffusion. *arXiv preprint arXiv:2505.10994*, 2025.

570

571 Lei Chen, Chandan Setty, Haoyu Hu, Maia G. Vergniory, Sarah E. Grefe, Lukas Fischer, Xinlin  
 572 Yan, Gaku Eguchi, Andrey Prokofiev, Silke Paschen, Jennifer Cano, and Qimiao Si. Topo-  
 573 logical semimetal driven by strong correlations and crystalline symmetry. *Nature Physics*, 18  
 574 (11):1341–1346, September 2022. ISSN 1745-2481. doi: 10.1038/s41567-022-01743-4. URL  
 575 <http://dx.doi.org/10.1038/s41567-022-01743-4>.

576

577 Ricky T. Q. Chen and Yaron Lipman. Flow matching on general geometries, 2024. URL <https://arxiv.org/abs/2302.03660>.

578

579 Daniel W Davies, Keith T Butler, Adam J Jackson, Jonathan M Skelton, Kazuki Morita, and Aron  
 580 Walsh. Smact: Semiconducting materials by analogy and chemical theory. *Journal of Open*  
 581 *Source Software*, 4(38):1361, 2019.

582

583 Scott Fredericks, Kevin Parrish, Dean Sayre, and Qiang Zhu. Pyxtal: A python library for crystal  
 584 structure generation and symmetry analysis. *Computer Physics Communications*, 261:107810,  
 585 April 2021. ISSN 0010-4655. doi: <https://doi.org/10.1016/j.cpc.2020.107810>. URL <http://www.sciencedirect.com/science/article/pii/S0010465520304057>.

586

587 Colin W Glass, Artem R Oganov, and Nikolaus Hansen. Uspex—evolutionary crystal structure  
 588 prediction. *Computer physics communications*, 175(11-12):713–720, 2006.

589

590 Rhys EA Goodall and Alpha A Lee. Predicting materials properties without crystal structure: Deep  
 591 representation learning from stoichiometry. *Nature Communications*, 11(1):1–9, 2020.

592

593 Rhys EA Goodall, Abhijith S Parackal, Felix A Faber, Rickard Armiento, and Alpha A Lee.  
 594 Rapid discovery of stable materials by coordinate-free coarse graining. *Science Advances*, 8  
 595 (30):eabn4117, 2022.

594 Philipp Hoellmer, Thomas Egg, Maya M. Martirosyan, Eric Fuemmeler, Zeren Shui, Amit Gupta,  
 595 Pawan Prakash, Adrian Roitberg, Mingjie Liu, George Karypis, Mark Transtrum, Richard G.  
 596 Hennig, Ellad B. Tadmor, and Stefano Martiniani. Open materials generation with stochastic  
 597 interpolants, 2025. URL <https://arxiv.org/abs/2502.02582>.

598 Anubhav Jain, Shyue Ping Ong, Geoffroy Hautier, Wei Chen, William Davidson Richards, Stephen  
 599 Dacek, Shreyas Cholia, Dan Gunter, David Skinner, Gerbrand Ceder, and Kristin A. Persson.  
 600 The Materials Project: A materials genome approach to accelerating materials innovation. *APL  
 601 Materials*, 1(1):011002, 07 2013. ISSN 2166-532X. doi: 10.1063/1.4812323. URL <https://doi.org/10.1063/1.4812323>.

603 Rui Jiao, Wenbing Huang, Peijia Lin, Jiaqi Han, Pin Chen, Yutong Lu, and Yang Liu. Crystal  
 604 structure prediction by joint equivariant diffusion. *arXiv preprint arXiv:2309.04475*, 2023. URL  
 605 <https://arxiv.org/abs/2309.04475>.

606 Rui Jiao, Wenbing Huang, Yu Liu, Deli Zhao, and Yang Liu. Space group constrained crystal  
 607 generation, 2024. URL <https://arxiv.org/abs/2402.03992>.

609 Chaitanya K. Joshi, Xiang Fu, Yi-Lun Liao, Vahe Gharakhanyan, Benjamin Kurt Miller, Anuroop  
 610 Sriram, and Zachary W. Ulissi. All-atom diffusion transformers: Unified generative modelling of  
 611 molecules and materials, 2025. URL <https://arxiv.org/abs/2503.03965>.

613 Nikita Kazeev, Wei Nong, Ignat Romanov, Ruiming Zhu, Andrey Ustyuzhanin, Shuya Yamazaki,  
 614 and Kedar Hippalgaonkar. Wyckoff transformer: Generation of symmetric crystals, 2025. URL  
 615 <https://arxiv.org/abs/2503.02407>.

616 Filip Ekström Kelvinius, Oskar B Andersson, Abhijith S Parackal, Dong Qian, Rickard Armiento,  
 617 and Fredrik Lindsten. Wyckoffdiff—a generative diffusion model for crystal symmetry. *arXiv  
 618 preprint arXiv:2502.06485*, 2025.

619 Diederik P Kingma and Jimmy Ba. Adam: A method for stochastic optimization. *arXiv preprint  
 620 arXiv:1412.6980*, 2014.

622 Scott Kirklin, James E Saal, Bryce Meredig, Alex Thompson, Jeff W Doak, Muratahan Aykol,  
 623 Stephan Rühl, and Chris Wolverton. The open quantum materials database (oqmd): assessing the  
 624 accuracy of dft formation energies. *npj Computational Materials*, 1(1):1–15, 2015.

625 Jonas Köhler, Leon Klein, and Frank Noé. Equivariant flows: Exact likelihood generative learn-  
 626 ing for symmetric densities. In *Proceedings of the 37th International Conference on Machine  
 627 Learning, ICML’20*. JMLR.org, 2020.

629 Jonas Köhler, Michele Invernizzi, Pim De Haan, and Frank Noé. Rigid body flows for sampling  
 630 molecular crystal structures. In *International Conference on Machine Learning*, pp. 17301–  
 631 17326. PMLR, 2023.

632 Georg Kresse and Jürgen Furthmüller. Efficient iterative schemes for ab initio total-energy calcula-  
 633 tions using a plane-wave basis set. *Physical review B*, 54(16):11169, 1996.

634 Minoru Kusaba, Chang Liu, and Ryo Yoshida. Crystal structure prediction with machine learning-  
 635 based element substitution. *Computational Materials Science*, 211:111496, 2022.

637 Daniel Levy, Siba Smarak Panigrahi, Sékou-Oumar Kaba, Qiang Zhu, Kin Long Kelvin Lee,  
 638 Mikhail Galkin, Santiago Miret, and Siamak Ravanbakhsh. Symmcld: Symmetry-preserving  
 639 crystal generation with diffusion models, 2025. URL <https://arxiv.org/abs/2502.03638>.

641 Peijia Lin, Pin Chen, Rui Jiao, Qing Mo, Cen Jianhuan, Wenbing Huang, Yang Liu, Dan Huang,  
 642 and Yutong Lu. Equivariant diffusion for crystal structure prediction. In *Forty-first International  
 643 Conference on Machine Learning*, 2024. URL <https://openreview.net/forum?id=VRv8KjJNu.j>.

645 Yaron Lipman, Ricky TQ Chen, Heli Ben-Hamu, Maximilian Nickel, and Matthew Le. Flow match-  
 646 ing for generative modeling. In *The Eleventh International Conference on Learning Representa-  
 647 tions*, 2022.

648 Yaron Lipman, Marton Havasi, Peter Holderrieth, Neta Shaul, Matt Le, Brian Karrer, Ricky T. Q.  
 649 Chen, David Lopez-Paz, Heli Ben-Hamu, and Itai Gat. Flow matching guide and code, 2024.  
 650 URL <https://arxiv.org/abs/2412.06264>.

651 Xingchao Liu, Chengyue Gong, and Qiang Liu. Flow straight and fast: Learning to generate and  
 652 transfer data with rectified flow. *arXiv preprint arXiv:2209.03003*, 2022.

653 Cécile Malgrange, Christian Ricolleau, and Michel Schlenker. *Symmetry and physical properties of*  
 654 *crystals*. Springer, 2014.

655 Amil Merchant, Simon Batzner, Samuel S Schoenholz, Muratahan Aykol, Gowoon Cheon, and  
 656 Ekin Dogus Cubuk. Scaling deep learning for materials discovery. *Nature*, pp. 1–6, 2023.

657 Mila AI4Science, Alex Hernandez-Garcia, Alexandre Duval, Alexandra Volokhova, Yoshua Ben-  
 658 gio, Divya Sharma, Pierre Luc Carrier, Michał Koziarski, and Victor Schmidt. Crystal-GFN:  
 659 sampling crystals with desirable properties and constraints. *AI for Accelerated Materials Design*  
 660 *Workshop (NeurIPS)*, 2023.

661 Benjamin Kurt Miller, Ricky T. Q. Chen, Anuroop Sriram, and Brandon M Wood. Flowmm: Gen-  
 662 erating materials with riemannian flow matching, 2024. URL <https://arxiv.org/abs/2406.04713>.

663 Shyue Ping Ong, William Davidson Richards, Anubhav Jain, Geoffroy Hautier, Michael Kocher,  
 664 Shreyas Cholia, Dan Gunter, Vincent L Chevrier, Kristin A Persson, and Gerbrand Ceder. Python  
 665 materials genomics (pymatgen): A robust, open-source python library for materials analysis.  
 666 *Computational Materials Science*, 68:314–319, 2013.

667 John P Perdew, Kieron Burke, and Matthias Ernzerhof. Generalized gradient approximation made  
 668 simple. *Physical review letters*, 77(18):3865, 1996.

669 Chris J. Pickard. Airss data for carbon at 10gpa and the c+n+h+o system at 1gpa. *Materials Cloud*  
 670 *Archive*, 2020.0026/v1, 2020. doi: 10.24435/materialscloud:2020.0026/v1.

671 Chris J Pickard and RJ Needs. Ab initio random structure searching. *Journal of Physics: Condensed*  
 672 *Matter*, 23(5):053201, 2011.

673 Omri Puny, Matan Atzmon, Heli Ben-Hamu, Edward J Smith, Ishan Misra, Aditya Grover, and  
 674 Yaron Lipman. Frame averaging for invariant and equivariant network design. *Tenth International*  
 675 *Conference on Learning Representations (ICLR)*, 2021.

676 Danilo Jimenez Rezende, Sébastien Racanière, Irina Higgins, and Peter Toth. Equivariant hamilton-  
 677 ian flows, 2019. URL <https://arxiv.org/abs/1909.13739>.

678 James E Saal, Scott Kirklin, Muratahan Aykol, Bryce Meredig, and Christopher Wolverton. Ma-  
 679 terials design and discovery with high-throughput density functional theory: the open quantum  
 680 materials database (oqmd). *Jom*, 65(11):1501–1509, 2013.

681 Victor Garcia Satorras, Emiel Hoogeboom, and Max Welling. E(n) equivariant graph neural net-  
 682 works, 2022. URL <https://arxiv.org/abs/2102.09844>.

683 Jonathan Schmidt, Noah Hoffmann, Hai-Chen Wang, Pedro Borlido, Pedro JMA Carriço, Tiago FT  
 684 Cerqueira, Silvana Botti, and Miguel AL Marques. Large-scale machine-learning-assisted explo-  
 685 ration of the whole materials space. *arXiv preprint arXiv:2210.00579*, 2022a.

686 Jonathan Schmidt, Hai-Chen Wang, Tiago FT Cerqueira, Silvana Botti, and Miguel AL Marques. A  
 687 dataset of 175k stable and metastable materials calculated with the pbesol and scan functionals.  
 688 *Scientific Data*, 9(1):64, 2022b.

689 Yuxuan Song, Jingjing Gong, Minkai Xu, Ziyao Cao, Yanyan Lan, Stefano Ermon, Hao Zhou,  
 690 and Wei-Ying Ma. Equivariant flow matching with hybrid probability transport, 2023. URL  
 691 <https://arxiv.org/abs/2312.07168>.

692 Anuroop Sriram, Benjamin Kurt Miller, Ricky T. Q. Chen, and Brandon M. Wood. Flowilm: Flow  
 693 matching for material generation with large language models as base distributions, 2024. URL  
 694 <https://arxiv.org/abs/2410.23405>.

702 Feng Tang, Hoi Chun Po, Ashvin Vishwanath, and Xiangang Wan. Comprehensive search for topo-  
 703 logical materials using symmetry indicators. *Nature*, 566(7745):486–489, February 2019. ISSN  
 704 1476-4687. doi: 10.1038/s41586-019-0937-5. URL <http://dx.doi.org/10.1038/s41586-019-0937-5>.

705

706 Hai-Chen Wang, Silvana Botti, and Miguel AL Marques. Predicting stable crystalline compounds  
 707 using chemical similarity. *npj Computational Materials*, 7(1):12, 2021.

708

709 Peter Wirsberger, George Papamakarios, Borja Ibarz, Sébastien Racanière, Andrew J Ballard,  
 710 Alexander Pritzel, and Charles Blundell. Normalizing flows for atomic solids. *Machine Learning: Science and Technology*, 3(2):025009, 2022.

711

712 Zhenqin Wu, Bharath Ramsundar, Evan N Feinberg, Joseph Gomes, Caleb Geniesse, Aneesh S  
 713 Pappu, Karl Leswing, and Vijay Pande. Moleculenet: a benchmark for molecular machine learning.  
 714 *Chemical science*, 9(2):513–530, 2018.

715

716 Tian Xie, Xiang Fu, Octavian-Eugen Ganea, Regina Barzilay, and Tommi S Jaakkola. Crystal  
 717 diffusion variational autoencoder for periodic material generation. In *International Conference on Learning Representations*, 2021. URL <https://arxiv.org/abs/2110.06197>.

718

719 Keqiang Yan, Alexandra Saxton, Xiaofeng Qian, Xiaoning Qian, and Shuiwang Ji. A space group  
 720 symmetry informed network for  $O(3)$  equivariant crystal tensor prediction, 2024. URL <https://arxiv.org/abs/2406.12888>.

721

722 Keqiang Yan, Xiner Li, Hongyi Ling, Kenna Ashen, Carl Edwards, Raymundo Arróyave, Marinka  
 723 Zitnik, Heng Ji, Xiaofeng Qian, Xiaoning Qian, and Shuiwang Ji. Invariant tokenization of crystalline  
 724 materials for language model enabled generation, 2025. URL <https://arxiv.org/abs/2503.00152>.

725

726

727 Jiashi Yang. *An introduction to the theory of piezoelectricity*. Springer, 2005.

728

729 Mengjiao Yang, KwangHwan Cho, Amil Merchant, Pieter Abbeel, Dale Schuurmans, Igor Mor-  
 730 datch, and Ekin Dogus Cubuk. Scalable diffusion for materials generation. *arXiv preprint arXiv:2311.09235*, 2023.

731

732 Dmitry Yarotsky. Universal approximations of invariant maps by neural networks. *Constructive  
 733 Approximation*, 55(1):407–474, 2022.

734

735 Jason Yim, Andrew Campbell, Andrew YK Foong, Michael Gastegger, José Jiménez-Luna, Sarah  
 736 Lewis, Victor Garcia Satorras, Bastiaan S Veeling, Regina Barzilay, Tommi Jaakkola, et al. Fast  
 737 protein backbone generation with  $se(3)$  flow matching. *arXiv preprint arXiv:2310.05297*, 2023.

738

739 Claudio Zeni, Robert Pinsler, Daniel Zügner, Andrew Fowler, Matthew Horton, Xiang Fu, Sasha  
 740 Shysheya, Jonathan Crabbé, Lixin Sun, Jake Smith, et al. Mattergen: a generative model for  
 741 inorganic materials design. *arXiv preprint arXiv:2312.03687*, 2023. URL <https://arxiv.org/abs/2312.03687>.

742

743 Ruiming Zhu, Wei Nong, Shuya Yamazaki, and Kedar Hippalgaonkar. Wycryst: Wyckoff inorganic  
 744 crystal generator framework. *Matter*, 7(10):3469–3488, 2024.

745

## A PROOFS

### A.1 PROOF OF THEOREM 3.2

747 *Proof.* The proof has two main parts. First, we will show that the flow  $\psi_t$  defined by the  $G$ -  
 748 equivariant vector field  $u_t$  is  $G$ -equivariant. Then, we will use this property to demonstrate that  
 749 the resulting probability path  $p_t$  is  $G$ -invariant. As a reminder, the flow  $\psi : [0, 1] \times \mathcal{X} \rightarrow \mathcal{X}$  is  
 750 defined by the following ODE:

$$\frac{d}{dt} \psi_t(x) = u_t(\psi_t(x)) \tag{11}$$

$$\psi_0(x) = x \tag{12}$$

To demonstrate that  $\psi_t$  is equivariant, we will show that two functions,  $\varphi_t(x) := \psi_t(g \cdot x)$  and  $\phi_t(x) = g \cdot \psi_t(x)$  (for arbitrary  $g \in G$ ) satisfy the same ODE with identical initial conditions.

$$\begin{aligned} \frac{d}{dt} \varphi_t(x) &= \frac{d}{dt} \psi_t(g \cdot x) = u_t(\psi_t(g \cdot x)) = u_t(\varphi_t(x)) \\ \varphi_0(x) &= \psi_0(g \cdot x) = g \cdot x \end{aligned}$$

$$\begin{aligned} \frac{d}{dt} \phi_t(x) &= \frac{d}{dt} g \cdot \psi_t(x) = g \cdot \frac{d}{dt} \psi_t(x) = g \cdot u_t(\psi_t(x)) = u_t(g \cdot \psi_t(x)) = u_t(\phi_t(x)) \\ \phi_0(x) &= g \cdot \psi_0(x) = g \cdot x \end{aligned}$$

Where the forth equality uses the  $G$ -equivariance of  $u_t$ . We can therefore conclude  $\psi_t(g \cdot x) = g \cdot \psi_t(x)$  for every  $x \in \mathcal{X}$ ,  $g \in G$  and  $t \in [0, 1]$ , which prove that  $\psi_t$  is  $G$ -equivariant.

It remains to show that  $p_t$  defines an invariant probability path.

$$\begin{aligned} p_t(g \cdot x) &= p_0(\psi_t^{-1}(g \cdot x)) \det \left[ \frac{\partial \psi_t^{-1}}{\partial x}(g \cdot x) \right] \\ &= p_0(\psi_t^{-1}(x)) \det \left[ \frac{\partial \psi_t^{-1}}{\partial x}(g \cdot x) \right] \\ &= p_0(\psi_t^{-1}(x)) \det \left[ g \cdot \frac{\partial \psi_t^{-1}}{\partial x}(x) \cdot g^{-1} \right] \\ &= p_0(\psi_t^{-1}(x)) \det \left[ \frac{\partial \psi_t^{-1}}{\partial x}(x) \right] = p_t(x) \end{aligned}$$

The second equality follows from the  $G$ -equivariance of  $\psi_t^{-1}$  and the  $G$ -invariance of  $p_0$ . The third equality is a consequence of the definition of the Jacobian matrix for equivariant functions, and the final equality relies on standard properties of the determinant.

## A.2 PROOF OF THEOREM 3.4

*Proof.* The first part of the proof, which involves showing that  $\psi_t$  is  $G$ -symmetric, is straightforward and follows directly from the equivariance properties of  $\psi_t$ . Since  $\psi_t$  is  $G \times S_n$  (and the group actions commute) it trivial to see that it is equivariant to each of the groups separately. Let the  $g \in G$  then:

$$g \cdot \psi_t(c) = \psi_t(g \cdot c) = \psi_t(\sigma \cdot c) = \sigma \cdot \psi_t(c)$$

Where the first equality follows from the  $G$ -equivariance of  $\psi_t$ , the second holds because  $c$  is  $G$ -symmetric, and the final equality follows from the  $S_n$ -equivariance of  $\psi_t$ . From the above equation, we also conclude that  $c$  and  $\psi_t(c)$  are mutually  $G$ -symmetric. Now, let  $g' \in G_{f_i}$ , meaning the  $g'$  belongs to the site-symmetry group of  $f_i$ , the  $i^{\text{th}}$  fractional coordinate of  $c$ . Since  $g' \in G$  there exist a permutation  $\sigma' \in S_n$  s.t  $g' \cdot c = \sigma' \cdot c$ . Moreover, because  $g' \in G_{f_i}$ , the permutation must fix the index  $i$ ,  $\sigma'(i) = i$ . From the previous part of the proof, we know that  $g' \cdot \psi_t(c) = \sigma' \cdot \psi_t(c)$  and since  $\sigma'(i) = i$ , it follows that  $g' \in G_{f'_i}$ , where  $f'_i$  is the  $i^{\text{th}}$  fractional coordinate of  $\psi_t(c)$ . Therefore,  $\psi_t(c)$  retains the same site-symmetry structure as  $c$ , and is thus also  $\mathcal{W}$ -constructable.  $\square$

## A.3 PROOF OF THEOREM 3.1

let  $g \in G$ , our goal is to show that there exists a permutation  $\sigma \in S_n$  such that  $g \cdot \mathbf{F}_0 = \sigma \cdot \mathbf{F}_0$ . Since  $\mathbf{F}_0$  is  $\mathcal{W}$ -constructable it can be written as a union of orbits under the action of  $G$ . Focusing on a single orbit generated by  $w_i$ , and denote it as  $\mathbf{F}_0^{w_i}$  we can observe that  $g \cdot \mathbf{F}_0^{w_i} = \sigma' \cdot \mathbf{F}_0^{w_i}$  for some  $\sigma' \in S_{|w_i|}$ . This holds because the action of a group element on an orbit is a bijection. Repeating this process for each orbit contained in  $\mathbf{F}_0$  yields a construction for the permutation  $\sigma$ .  $\square$

810 A.4 PROOF OF THEOREM 3.5  
811812 *Proof.*

813 
$$\hat{u}_t(c|G) = \sum_{g \in G} g \cdot u_t(g^{-1} \cdot c) = \sum_{g \in G} g \cdot u_t(\sigma_{g^{-1}|c} \cdot c) = \sum_{g \in G} g \cdot \sigma_{g^{-1}|c} \cdot u_t(c)$$
  
814  
815

816 the second equation comes from the  $G$ -symmetry of  $c$  and the last comes from the  $S_n$  equivariance  
817 of  $u_t$ .  $\square$ 818 B CONDITIONAL FLOW ON FRACTIONAL COORDINATES  
819820 **Lemma B.1.** *Let  $G$  be a space group, the flat tori logarithmic map  $\log_{\mathbf{F}_0}(\mathbf{F}_1)$  is  $G \times S_n$  equivariant.*821  
822 *Proof.* let  $g \in G$  such that  $g = (\mathbf{R}, \tau)$ . Since the orthogonal components of  $G$  maps the crystal to  
823 itself, it preserve the lattice structure. combining with the following lemma (which is expressed with  
824 respect to a single point) we get that logarithmic maps is equivariant with respect to the space group  
825 and that the representation acts on the output domain includes only the orthogonal part without  
826 the translation. The  $S_n$  equivariance is trivial for an element wise function.  $\square$ 827  
828 **Lemma B.2.** *Let  $g \in G$  such that  $g = (\mathbf{R}, \tau)$ . if  $\mathbf{R}$  maps  $\mathbb{Z}^3$  to itself  $\mathbf{R} \log_x(y) = \log_{g \cdot x}(g \cdot y)$ .*829  
830 *Proof.* Let  $\log_x(y) = v$  that means that exist  $z \in \mathbb{Z}^3$  s.t  $v = y - x + z$  where  $v \in [-\frac{1}{2}, \frac{1}{2})^3$ . Now  
831 lets assume  $\log_{g \cdot x}(g \cdot y) = v'$ , that means that there exist  $z' \in \mathbb{Z}^3$  s.t  $v' = g \cdot y - g \cdot x + z'$ . plugging  
832 in  $g = (\mathbf{R}, \tau)$  results in  $v' = \mathbf{R}(y - x) + z'$ . combining both equations we get that  $v' = \mathbf{R}v + z''$   
833 (because  $\mathbf{R}z \in \mathbb{Z}^3$ ). Since  $v' \in [-\frac{1}{2}, \frac{1}{2})^3$  and  $\|v\| = \|\mathbf{R}v\|$  we conclude that  $v' = \mathbf{R}v$ .  
834835  
836 **Lemma B.3.** *The conditional flow  $\psi_t(\mathbf{F}_0|\mathbf{F}_1)$  is  $G$ -symmetric and  $\mathcal{W}$ -constructable.*837  
838 *Proof.*

839 
$$\begin{aligned} g \cdot \psi_t(\mathbf{F}_0|\mathbf{F}_1) &= (\mathbf{F}_0 + t \log_{\mathbf{F}_0}(\mathbf{F}_1)) \mathbf{R}^T + \mathbf{1}_n \tau^T \\ 840 &= \mathbf{F}_0 \mathbf{R}^T + \mathbf{1}_n \tau^T + t \log_{\mathbf{F}_0}(\mathbf{F}_1) \mathbf{R}^T \\ 841 &= g \cdot \mathbf{F}_0 + t \log_{g \cdot \mathbf{F}_0}(g \cdot \mathbf{F}_1) \\ 842 &= \sigma \cdot \mathbf{F}_0 + t \log_{\sigma \cdot \mathbf{F}_0}(\sigma \cdot \mathbf{F}_1) \\ 843 &= \sigma \cdot \psi_t(\mathbf{F}_0|\mathbf{F}_1) \end{aligned}$$
  
844  
845

846 The fact that  $\psi_t(\mathbf{F}_0|\mathbf{F}_1)$  is  $\mathcal{W}$ -constructable follows directly from the proof in appendix A.2 and the  
847 fact the  $\psi_t(\mathbf{F}_0|\mathbf{F}_1)$  is mutually  $G$ -symmetric with  $\mathbf{F}_0$  and  $\mathbf{F}_1$ .  $\square$ 848 C LATTICE REPRESENTATION  
849850  
851 The lattice matrix  $\mathbf{L} \in \mathbb{R}^{3 \times 3}$  characterizes the geometry of the unit cell. When  $\mathbf{L}$  corresponds to  
852 a physically valid lattice, i.e., it has positive volume, it is invertible and can be decomposed to the  
853 product  $\mathbf{L} = \mathbf{Q} \exp(\mathbf{S})$  where  $\mathbf{Q} \in \mathbb{R}^{3 \times 3}$  is an orthogonal matrix and  $\mathbf{S} \in \mathbb{R}^{3 \times 3}$  is a symmetric  
854 matrix. Representing the lattice parameters via  $\mathbf{S}$  enjoys the benefits of orthogonal invariance (any  
855 orthogonal transformation is added to  $\mathbf{Q}$ ), which makes this representation invariant to any space  
856 group operations. Jiao et al. (2024) suggested representing  $\mathbf{S}$  using the coefficients of the following  
857 basis -

858 
$$\begin{aligned} \mathbf{B}_1 &= \begin{pmatrix} 0 & 1 & 0 \\ 1 & 0 & 0 \\ 0 & 0 & 0 \end{pmatrix}, \mathbf{B}_2 = \begin{pmatrix} 0 & 0 & 1 \\ 0 & 0 & 0 \\ 1 & 0 & 0 \end{pmatrix}, \mathbf{B}_3 = \begin{pmatrix} 0 & 0 & 0 \\ 0 & 0 & 1 \\ 0 & 1 & 0 \end{pmatrix}, \\ 859 & \mathbf{B}_4 = \begin{pmatrix} 1 & 0 & 0 \\ 0 & -1 & 0 \\ 0 & 0 & 0 \end{pmatrix}, \mathbf{B}_5 = \begin{pmatrix} 1 & 0 & 0 \\ 0 & 1 & 0 \\ 0 & 0 & -2 \end{pmatrix}, \mathbf{B}_6 = \begin{pmatrix} 1 & 0 & 0 \\ 0 & 1 & 0 \\ 0 & 0 & 1 \end{pmatrix}. \end{aligned}$$
  
860  
861  
862  
863

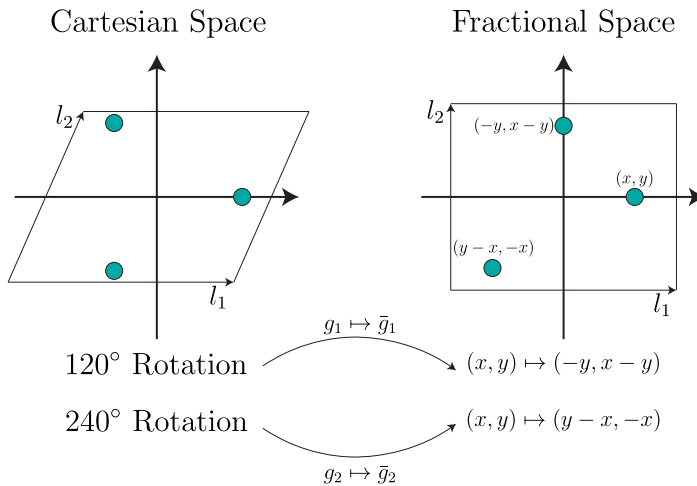


Figure 5: 2D visualization of the deformed geometry induced by moving to fractional coordinates in a non-orthogonal lattice basis. This example demonstrates how a 3-fold rotational space group becomes a set of special affine transformations when acting on fractional coordinates *and, specifically, the mapping of each rotation element to a corresponding special affine transformation*. In addition, the figure illustrates how a space group induced orbit transforms under this change of basis. This new representation makes it difficult to use models that rely on Euclidean geometry.

This basis enables clustering of the crystallographic space groups based on the basis coefficients used to represent  $S$ . Table 5 summarizes the lattice and coefficient constraints for each crystal family type.

Table 5: Relationship between the lattice shape and the constraint of the symmetric bases.

Crystal Family	Space Group No.	Lattice Shape	Constraint of Symmetric Bases
Triclinic	1 ~ 2	No Constraint	No Constraint
Monoclinic	3 ~ 15	$\alpha = \gamma = 90^\circ$	$k_1 = k_3 = 0$
Orthorhombic	16 ~ 74	$\alpha = \beta = \gamma = 90^\circ$	$k_1 = k_2 = k_3 = 0$
Tetragonal	75 ~ 142	$\alpha = \beta = \gamma = 90^\circ$ $a = b$	$k_1 = k_2 = k_3 = 0$ $k_4 = 0$
Hexagonal	143 ~ 194	$\alpha = \beta = 90^\circ, \gamma = 120^\circ$ $a = b$	$k_2 = k_3 = 0, k_1 = -\log(3)/4$ $k_4 = 0$
Cubic	195 ~ 230	$\alpha = \beta = \gamma = 90^\circ$ $a = b = c$	$k_1 = k_2 = k_3 = 0$ $k_4 = k_5 = 0$

## D DENSITY FUNCTIONAL THEORY

Crystals exist in competition for stability between alternatives with the same composition. If one plots energy against composition, the lowest energy structures form a *convex hull*. We say a crystal is thermodynamically stable if it is near or below this convex hull. Since we do not know all structures, there is epistemic uncertainty in this characterization. The difference between the energy of a crystal and this convex hull is denoted  $E_{\text{hull}}$ . We report  $E_{\text{hull}} < 100$  meV/atom and  $E_{\text{hull}} < 0$  meV/atom rates for stability metrics. These values are computed by prerelaxation with a machine learning interatomic potential (Barroso-Luque et al., 2024) followed by relaxation and energy evaluation using density functional theory.

918 For the stability metrics, we applied the Vienna ab initio simulation package (VASP) (Kresse &  
 919 Furthmüller, 1996) to compute relaxed geometries and ground state energies at a temperature of  
 920 0 K and pressure of 0 atm. We used the default settings from the Materials Project (Jain et al.,  
 921 2013) known as the MPRelaxSet with the PBE functional (Perdew et al., 1996) and Hubbard U  
 922 corrections. These correspond with the settings that our prerelaxation network OMat24 (Barroso-  
 923 Luque et al., 2024) was trained on, so prerelaxation should reduce DFT energy, up to fitting error.

924 We did *not* make any guesses about oxidation states! This deviates from the Materials Project which  
 925 does make those guesses. For this reason, our energy above hull calculations for structures that need  
 926 to consider oxidation state are slightly high, implying that we might be under-predicting stability.  
 927 This applies to any stability result we calculated. We expect it to also be a negligible effect.

928 The results from DiffCSP++ WyFormer in table 3 were computed by Kazeev et al. (2025) and differ  
 929 slightly from ours. Specifically, they run a multiple relaxations to avoid errors that come from  
 930 using a poor initial guess before relaxation. Since we prerelax with OMat24 we expect that double  
 931 relaxation is unnecessary. Consult their work for further details, but we believe the differences are  
 932 negligible for this purpose.

## 935 E RELATED WORK

936 As a continuation from section 5, we discuss other related work. We still limit the focus to the  
 937 most-relevant parts of this large body of literature.

938 Our method resembles non-deep learning based methods that propose structures using Wyckoff po-  
 939 sitions as inductive bias (Glass et al., 2006; Pickard & Needs, 2011) and refine the atomic positions  
 940 using density functional theory. This field is known as high-throughput screening of inorganic crys-  
 941 tals and it is responsible for generating several important datasets of stable materials (Saal et al.,  
 942 2013; Kirklin et al., 2015; Wang et al., 2021; Schmidt et al., 2022a;b). Recently, those searches have  
 943 been sped up by machine learning interatomic potentials that closely approximate density functional  
 944 theory (Merchant et al., 2023).

945 Now we take a step further away conceptually to discuss methods that are tangentially related to  
 946 ours. *Crystal-GFN* (Mila AI4Science et al., 2023) is a G-flow network that uses the space group,  
 947 but does not consider Wyckoff positions. *Mat2Seq* (Yan et al., 2025) proposes a one-dimensional  
 948 sequence representation of crystal structures that embeds space group information. *GMTNet* (Yan  
 949 et al., 2024) enforces space group invariance in a crystal property prediction model. Several other  
 950 works generate crystals without considering multiple types of atom (Wirnsberger et al., 2022), or  
 951 molecule (Köhler et al., 2023). Additionally, there is a large and growing cannon of generative  
 952 models for materials that do not have general space group equivariance (Xie et al., 2021; Yang et al.,  
 953 2023; Zeni et al., 2023; Miller et al., 2024; Sriram et al., 2024; Lin et al., 2024; Joshi et al., 2025;  
 954 Hoellmer et al., 2025).

## 955 F BASELINES

956 We provide additional context on the core approach behind each baseline we compared against:  
 957 *CDVAE*, integrates a diffusion model with a variational autoencoder for crystal structure generation;  
 958 *AdiT*, which use latent-based diffusion model and train on additional information from the QM9  
 959 (Wu et al., 2018) dataset; *FlowMM*, an application of Riemannian Flow Matching (Chen & Lip-  
 960 man, 2024) that incorporates non-trivial geometries in the crystal representation space; *FlowLLM*,  
 961 combines FlowMM with a Large Language model that uses as base distribution generator. *OMatG*,  
 962 leverages Stochastic Interpolants (Albergo et al., 2023) for material generation; *SymmCD*, operates  
 963 on the asymmetric unit and incorporates Wyckoff positions as part of the generative process; *Dif-  
 964 fCSP++*, a diffusion-based model that conditions on space groups and projects each denoising step  
 965 through Wyckoff position transformations; *WyFormer*, which employs an autoregressive model to  
 966 generate Wyckoff positions (conditioned on space group) and subsequently uses DiffCSP++ model  
 967 for full structure generation to predict the structure; and finally, *SGEquiDiff* a diffusion based model  
 968 that enforce space group equivariance while working on the asymmetric unit.

972 **G MODEL DETAILS**  
973974 **G.1 ARCHITECTURE**  
975

976 In this section, we present a comprehensive overview of our vector field model  $\hat{u}_t(\cdot | G)$ , along with  
977 the hyperparameters employed during training and generation across all experiments. The model  
978 takes as input a crystal  $c = (k, \mathbf{F}, \mathbf{A})$ , where  $f^i \in \mathbb{R}^3$  denotes the  $i^{\text{th}}$  fractional coordinate in  $\mathbf{F}$ ,  
979 and  $a^i \in \{0, 1\}^h$  represents the  $i^{\text{th}}$  atom type indicator vector in  $\mathbf{A}$ . The forward computation of  $s$   
980 layers model  $\hat{u}(c, |, G)$  is defined by the following set of equations:

$$\begin{aligned}
 981 \quad a_{\text{embed}}^i &= \phi^a(a^i) \\
 982 \quad t_{\text{embed}} &= \text{SinusoidalTimeEmbedding}(t) \\
 983 \quad h_{(0)}^i &= \phi^{\text{embed}}([a_{\text{embed}}^i, t_{\text{embed}}]) \\
 984 \quad m_{(l)}^{ij} &= \phi_{(l)}^{\text{edge}}\left(\left[h_{(l-1)}^i, h_{(l-1)}^j, k, \text{SinusoidalEmbedding}(\log_{f^i}(f^j)), \frac{L^T L \log_{f^i}(f^j)}{\|L^T L \log_{f^i}(f^j)\|}\right]\right) \\
 985 \quad m_{(l)}^i &= \frac{1}{n} \sum_{j=1}^n m_{(l)}^{ij} \\
 986 \quad h_{(l)}^i &= \phi_{(l)}^{\text{node}}\left(\left[h_{(l-1)}^i, m_{(l)}^i\right]\right) \\
 987 \quad u_t^k(c_t) &= \phi^k\left(\frac{1}{n} \sum_{j=1}^n h_{(s)}^i\right) \\
 988 \quad (u_t^{\mathbf{F}}(c_t))^i &= \phi^{\mathbf{F}}(h_{(s)}^i) \\
 989 \quad (u_t^{\mathbf{A}}(c_t))^i &= \phi^{\mathbf{A}}(h_{(s)}^i) \\
 990 \quad u_t(c_t) &= (u_t^k(c_t), u_t^{\mathbf{F}}(c_t), u_t^{\mathbf{A}}(c_t)) \\
 991 \quad \hat{u}_t(c_t | G) &= \sum_{g \in G} g \cdot \sigma_{g^{-1}|c} \cdot u_t(c_t)
 \end{aligned}$$

1003 We denote  $d$  as the hidden dimension of the model,  $d_t$  as the Sinusoidal Time Embedding dimension,  
1004 and  $d_s$  as the Sinusoidal Embedding dimension. Next, we list the learnable modules constructing the  
1005 model and denote their input and output dimension as  $x \rightarrow y$ .  $\phi^a$  is a linear layer  $h \rightarrow d$ ,  $\phi^{\text{embed}}$  is a  
1006 linear layer  $d + d_t \rightarrow d$  dimension  $d$ ,  $\phi_{(l)}^{\text{edge}}$  is 2-layer Multi-layer Perceptron (MLP)  $2d + d_t + 9 \rightarrow d$ ,  
1007  $\phi_{(l)}^{\text{node}}$  is a 2-layer Multi-layer Perceptron (MLP)  $2d \rightarrow d$ ,  $\phi^k$  is a linear layer  $d \rightarrow 6$ ,  $\phi^{\mathbf{F}}$  is a linear  
1008 layer  $d \rightarrow 3$  and  $\phi^{\mathbf{A}}$  is a linear layer  $d \rightarrow h$ . The last equation represents the group averaging  
1009 presented in eq. (4). The flat tori logarithmic map is defined by the equation:  
1010

$$1011 \quad \log_{f^i}(f^j) = \frac{1}{2\pi} \text{atan2}([\sin(f^j - f^i), \cos(f^j - f^i)]) \quad (13)$$

1012 Table 6 summarize the hyperparameters used to train our SGFM models. Note that the same con-  
1013 figuration was applied uniformly across all datasets and tasks. The hyperparameter search was  
1014 performed on MP-20 (CSP) and the resulting settings were adopted for all other experiments.  
1015

1016 **G.2 TRAINING & GENERATION**  
1017

1018 All of our models were trained using the ADAM optimizer (Kingma & Ba, 2014) on 8 NVIDIA A100  
1019 GPUs. Table 7 outlines the training configuration for each model, including the ranges explored during  
1020 hyperparameter search. We employed a cosine annealing learning rate schedule with a minimum  
1021 learning rate of 0.00001. As described in section 4, we applied inference anti-annealing to enhance  
1022 generation quality. This technique modifies the vector field by scaling it with a time-dependent func-  
1023 tion  $s(t) = 1 + s't$ , where  $s' \in \mathbb{R}^+$  is a hyperparameter. We defined separate annealing parameters  
1024 for each crystal component:  $s'_{\mathbf{F}}$  and  $s'_k$  (no annealing was applied to atom type prediction). For the  
1025 CSP experiments, we set  $s'_{\mathbf{F}} = 3$ ,  $s'_k = 3$ , and for DNG, we used  $s'_{\mathbf{F}} = 5$ ,  $s'_k = 3$ . Especially for  
Alex-MP-20 CSP we used  $s'_{\mathbf{F}} = 5$ ,  $s'_k = 3$ . All datasets have 60/20/20 train/validation/test split

1026  
 1027 Table 6: Hyperparameter details for all the models reported in the paper. Hyperparameter (bottom  
 1028 row) search was conducted on the MP-20 dataset.

1030 Dataset	Number of Layers	$d$	$d_t$	$d_s$	Activation	Layer Norm
CSP						
1032 MP-20	8	512	256	128	SiLU	✓
1033 MPTS-52	8	512	256	128	SiLU	✓
1034 Carbon-24	8	512	256	128	SiLU	✓
1035 Perov-5	8	512	256	128	SiLU	✓
1036 Alex-MP-20	8	512	256	128	SiLU	✓
DNG						
1037 MP-20	8	512	256	128	SiLU	✓
Hyperparameter Range						
1039 MP-20	{6, 7, 8, 9}	{128, 256, 512}	{128, 256}	{128, 256}	-	-

1041  
 1042 Table 7: Training hyperparameter details for all the models reported in the paper. Hyperparameter  
 1043 (bottom row) search was conducted per experiment.

1045 Dataset	Batch Size/GPU	Learning Rate	Epochs	$\lambda_F$	$\lambda_A$	$\lambda_k$
CSP						
1047 MP-20	64	0.0005	5000	100	-	1
MPTS-52	32	0.0005	5000	100	-	1
Carbon-24	64	0.0005	8000	100	-	1
Perov-5	256	0.0005	1000	100	-	1
Alex-MP-20	32	0.0003	1250	100	-	1
DNG						
1050 MP-20	64	0.0007	5000	100	1	1
Hyperparameter Range						
1052 -	-	{0.0002, 0.0005, 0.0007}	{1000, 1250, 2000, 5000, 8000}	{1, 10, 50, 100}	{1, 10, 50, 100}	{1, 10, 50, 100}

1053  
 1054 except Alex-MP-20 that has 80/10/10 split. We used the same split exact indexing split as OMatG  
 1055 to produce a train, test, and validation set (Hoellmer et al., 2025). OMatG derived its train/test split  
 1056 from MatterGen (Zeni et al., 2023) where it took 10% of the training data to make a validation set.  
 1057

### 1058 G.3 ATOM TYPE PREDICTION PROPERTIES

1059  
 1060 This section explains the properties of the atom-prediction component of  $\hat{u}(\cdot \mid G)$ . Specifically,  
 1061 it shows that when the input is a symmetric crystal  $c$ , the predicted atom-type vector field  
 1062  $\hat{u}^A(c \mid G)$  assigns identical values to atoms belonging to the same orbit. A point that may  
 1063 not be immediately obvious is that the group actions are defined in a similar way on the output  
 1064  $\hat{u}(c|G) = (\hat{u}^k(c|G), \hat{u}^F(c|G), \hat{u}^A(c|G))$  as they are defined over  $c$ , up to a representation, as dis-  
 1065 cussed in the section on fractional coordinates.

1066  
 1067 To begin with, we can show that  $\hat{u}^A(c \mid G)$  is  $G$ -invariant. On one hand, we know that  $\hat{u}^A(c \mid G) = \hat{u}^A(g \cdot c \mid G)$  because  $\hat{u}$  is  $G$ -equivariant and the group element  $g$  does not act directly on the  
 1068 atom-type component. Moreover, we also have  $\hat{u}^A(g \cdot c \mid G) = \hat{u}^A(\sigma_{g|c} \cdot c \mid G) = \sigma_{g|c} \cdot \hat{u}^A(c \mid G)$   
 1069 since  $\hat{u}$  is also  $S_n$ -equivariant and  $c$  is  $G$ -symmetric.

1070  
 1071 This relation,  $\hat{u}^A(c \mid G) = \sigma_{g|c} \cdot \hat{u}^A(c \mid G)$ , applies only to permutations corresponding to elements  
 1072 of the space group, which only permute atoms within the same orbit induced by the group action.  
 1073 Consequently, we can conclude that the atom-type vector field  $\hat{u}_t^A$  identifies on elements belonging  
 1074 to the same orbit.

### 1075 H RUNNING TIME ABLATIONS

1076  
 1077 This experimental ablation study aims to evaluate the efficiency of SGFM by comparing its per-  
 1078 formance during both training and generation against two baseline models: (1) a non-equivariant  
 1079 variant where the vector field does not incorporate group symmetry, and (2) a standard GA imple-

1080  
1081  
1082  
1083  
1084  
1085  
1086  
1087  
1088  
1089  
1090  
1091  
1092  
1093  
1094  
1095  
1096  
1097  
1098  
1099  
1100  
1101  
1102  
1103  
1104  
1105  
1106  
1107  
1108  
1109  
1110  
1111  
1112  
1113  
1114  
1115  
1116  
1117  
1118  
1119  
1120  
1121  
1122  
1123  
1124  
1125  
1126  
1127  
1128  
1129  
1130  
1131  
1132  
1133  
mentation as defined in eq. (3). For each model, we measured the time required to train a single epoch on MP-20, as well as the time needed to generate a batch of 64 (with 500 generation steps). The training time was averaged over 10 epochs, while the generation time was averaged over 100 batches. Training was conducted on an NVIDIA RTX8000 using 8 GPUs, while generation was performed on a single NVIDIA A10 GPU. The results are summarized in table 1. Due to memory constraints, the standard GA model was limited to a maximal batch size of 1 per GPU. **The generation results for the standard GA model were obtained from a randomly initialized model, as training such a model was intractable.** The results highlight a significant efficiency gap between the SGFM implementation of GA and the standard version, while showing minimal difference compared to the non-equivariant model.

## I LARGE LANGUAGE MODELS

We utilized of large language models (LLMs) to assist with language refinement and proofreading. No content, ideas, or analyses were produced by these tools. The usage was quite limited.